Gold nanoparticle-based brachytherapy enhancement in choroidal melanoma using a full Monte Carlo model of the human eye

Somayeh Asadi,[1a] Mehdi Vaez-zadeh,[1] S. Farhad Masoudi,[1] Faezeh Rahmani,[1] Courtney Knaup,[2] and Ali S. Meigooni[2]
Department of Physics,[1] K.N. Toosi University of Technology, Tehran, Iran; Comprehensive Cancer Centers of Nevada,[2] Las Vegas, NV, USA
s_asadi@sina.kntu.ac.ir

Received 20 January, 2015; accepted 8 April, 2015

The effects of gold nanoparticles (GNPs) in ^{125}I brachytherapy dose enhancement on choroidal melanoma are examined using the Monte Carlo simulation technique. Usually, Monte Carlo ophthalmic brachytherapy dosimetry is performed in a water phantom. However, here, the compositions of human eye have been considered instead of water. Both human eye and water phantoms have been simulated with MCNP5 code. These simulations were performed for a fully loaded 16 mm COMS eye plaque containing 13 ^{125}I seeds. The dose delivered to the tumor and normal tissues have been calculated in both phantoms with and without GNPs. Normally, the radiation therapy of cancer patients is designed to deliver a required dose to the tumor while sparing the surrounding normal tissues. However, as the normal and cancerous cells absorbed dose in an almost identical fashion, the normal tissue absorbed radiation dose during the treatment time. The use of GNPs in combination with radiotherapy in the treatment of tumor decreases the absorbed dose by normal tissues. The results indicate that the dose to the tumor in an eye-ball implanted with COMS plaque increases with increasing GNPs concentration inside the target. Therefore, the required irradiation time for the tumors in the eye is decreased by adding the GNPs prior to treatment. As a result, the dose to normal tissues decreases when the irradiation time is reduced. Furthermore, a comparison between the simulated data in an eye phantom made of water and eye phantom made of human eye composition, in the presence of GNPs, shows the significance of utilizing the composition of eye in ophthalmic brachytherapy dosimetry Also, defining the eye composition instead of water leads to more accurate calculations of GNPs radiation effects in ophthalmic brachytherapy dosimetry.

PACS number: 87.53.Jw, 87.85.Rs, 87.10.Rt

Key words: choroidal melanoma, brachytherapy, MCNP5, gold nanoparticles, dose enhancement

I. INTRODUCTION

Ocular melanoma or more specifically, uveal melanoma, is a malignant tumor which can arise from the melanin-producing cells or melanocytes residing within the uvea. These kinds of tumors have the highest rate of metastasis of any intraocular cancer. The method of treatment is determined according to the type of the cancer and the rate of its progress.[1-5] Enucleation, local resection, and radiation therapy are the most common methods of treatment for ocular melanoma.[6] In radiation therapy, penetrating radiation like X-ray, gamma ray, and alpha and

[a] Corresponding author: Somayeh Asadi, Department of Physics, K.N. Toosi University of Technology, Tehran, Iran. P.O.Box 15418-49611; email: s_asadi@sina.kntu.ac.ir

beta beams are used. These radiation types could be emitted from either a radiation apparatus such as linear accelerator or sealed radioactive sources (also known as brachytherapy sources) or from radio-labeled substances. Brachytherapy is a form of radiation therapy which involves placing small sealed radioactive seeds inside or adjacent to the tumor.[7-8] Studies have shown that, for most eye melanomas, the methods of using removable ophthalmic plaques loaded with brachytherapy sources are as effective as surgery (enucleation).[9-11]

Several isotopes, including ^{125}I and ^{103}Pd are used in the brachytherapy of choroidal melanoma.[12,13-14] Increasing the dose to the tumor, while decreasing the dose to the normal tissues remains as one of the biggest challenges in radiation therapy. Therefore, the design of the ophthalmic plaques and selection of the radionuclide for intraocular cancers has been the primary goal of the clinical studies for many investigators.[15-17] Several investigations based on Monte Carlo simulations or experimental techniques have been performed for dosimetry of choroidal melanoma, using different ophthalmic plaques containing various brachytherapy sources.[9,15,18-25]

Presently, there is increased interest in the potential use of gold nanoparticles (GNPs) as a dose enhancer in resolving the noted challenges in the treatment cancer patients through ionizing radiation.[17,26] In the context of such a treatment modalities, GNPs are considered to have advantageous characteristics such as biocompatibility, inertness, and no reported obvious toxicity.[27-28] High photon interaction cross section of gold resulting from its high atomic number and electron density increases the possibility of dose absorption by GNPs. Because of the strong photoelectric absorption and secondary electron released by low energy gamma-ray or X-ray irradiation, GNPs can increase in dose enhancement factor (DEF) which will accelerate DNA strand breaks.[29-31] DEF is defined as the ratio of the absorbed dose by the tumor containing GNPs to the absorbed dose by the tumor without these nanoparticles. In an *in vivo* study in mice bearing subcutaneous EMT-6 mammary carcinoma, Hainfeld et al.[32] demonstrated that the presence of GNPs in the tumor will cause more absorbed dose by the cancerous cells than that of the normal tissues. Irradiation stability and cytotoxicity of GNPs in human K562 cells have been investigated by Zhang et al.[26] and the results indicated that GNPs do not deteriorate under high energy ray irradiation and showed concentration-dependent cytotoxicity. Also, the toxicity of the nanoparticles have been examined via different ways of assessing the cell viability, like methyl thiazol tetrazolium (MTT) and Cell Titre-Glo Luminescent Cell Viability Assay[26,33] (Promega Corp., Madison, WI). In some of the *in vivo* and *in vitro* studies,[33-37] after intravenous injection of nanoparticles, transmission electron microscopy (TEM) demonstrated that GNPs are accumulated in clusters within the membrane-bound vesicles and lysosomes. The tumor vasculature shows more transmission than the normal blood vessels and there is no lymphatic drainage in the tumor. So, due to the poorly formed tumor vasculature, the accumulation of unlabeled nanoparticles within the tumor can occur under passive targeting by increasing the effect of permeability and retention (EPR).[38-39] Several other studies demonstrated the effects of GNPs in radiation treatment of the different tumors.[33,40-48]

A Monte Carlo study by Lechman et al.[45] was conducted to determine how the efficiency of gold nanoparticles in increasing radiation dose varies with the photon source energy, intercellular localization, size, and concentration of gold nanoparticles. The results showed that, when the energy of photon source is below the K-edge, GNPs localization becomes an increasingly important parameter in making dose enhancement in cells. In this case, the results suggest that, taken as an upper limit, the concentration of 5.39 mg per gram of tumor for GNPs with the size of 5 nm would be required per cell to increase the prescribed dose by a factor of 2. However, the size of GNPs is less crucial when the photon source energy is above the K-edge. But it requires significantly higher concentrations of GNPs. In an independent project by Leung et al.[46] using the MC technique, it was shown that gold nanoparticles with larger diameter and concentration increase the DEF in the tumor area. This means that, to obtain more precise results and knowing the parameters effective in cancer treatment by gold nanoparticles, more studies and examinations should be carried out.

Considerable advances have been made in the application of nanotechnology-based cancer therapy, and numerous studies have been carried out in this field through Monte Carlo simulation and experimental studies. However, only limited studies have been reported that relate eye tumors. From these resources, Sheng Zhang et al.[49] have studied the particles accumulation in the uveal tissue. In this report, the combination of nanoparticles of a suitable size with the ligands specified for the uveal melanoma cells has been found to be a good way for transferring these particles to the tumor area, which would help them to stay in the melanoma tissue for a long time. In addition, the authors reported that nanoparticles can escape through the uveal into the melanoma tissue with much higher accumulation than the microparticles with optimal sizes of 100 nm to 300 nm. In a different study, Kang et al.[50] have evaluated the efficacy of subconjunctival nanoparticles carboplatin in the murine retinoblastoma treatment. However, to our knowledge, the impact of the nanoparticles on the radiation dosimetry of the eye has not yet been evaluated. Therefore, this project has been designed to evaluate the enhancement of the absorbed dose by the presence of the GNPs within the human eye, considering both water and human eye compositions.

In this study we have investigated the application of GNPs in brachytherapy on the eye tumor by Monte Carlo simulations. These simulations are performed with the eye model phantom and water phantom (eye model filled with water) to determine the dose enhancement factor (DEF). In addition, the significance of the eye model on the DEF calculation has been evaluated by comparing the dosimetry calculations in the presence of GNPs in both eye model phantom and water phantom. These simulations are performed using MCNP5 Monte Carlo code. Dosimetric characteristics of a single source were utilized to validate the accuracy of the Monte Carlo simulation technique. Also, the dose distributions of the multisource implant geometry in both eye and water phantoms with 16 mm COMS standard eye plaque loaded with ^{125}I, model 6711 source (manufactured by GE Healthcare/Oncura; Waukesha, WI) have been simulated.

II. MATERIALS AND METHODS

A. Monte Carlo simulation

In this project, the MCNP5 code[51] has been utilized to evaluate the effect of GNPs on dose enhancement for treatment of ocular melanoma with ^{125}I eye plaque therapy. This code utilizes a three-dimensional heterogeneous geometry and transports for photons and electrons in the energy range from 1 KeV to 1 GeV. For the simulations of this project, the default MCNP5 photon cross-sectional library, which is based upon release 8 of the ENDF/B-VI[52] has been utilized. The simulations were performed with the *F8 tally for the phantom dosimetry and *F6 tally for the air kerma simulations. The photon energy cutoff is set to 5 KeV in this simulation. The calculated data in MeV per incident particle for each section of the phantom was then converted to absorbed dose (i.e., Gy) or absorbed dose rate per air kerma strength of the source (i.e., cGy $h^{-1}U^{-1}$) by introducing appropriate conversion factors following the published guidelines.[53-54] A number of $7*10^7$ and $2*10^9$ histories have been followed to simulate the air kerma and phantom dosimetry, respectively, in order to achieve a relative statistical error of less than 1%. Table 1 shows the error propagation of the Monte Carlo simulation with MCNP5 in this project.

The effects of the nanoparticles were calculated by performing the simulation in the eye model filled with the water and human eye composition, with and without the presence of the GNPs. Moreover, the geometric design of a 16 mm COMS standard eye plaque, loaded with 13 ^{125}I, model 6711 source, have been introduced in the simulations. The water phantom and the human eye globe geometries (Fig. 1) were designed in a manner similar to the one described in our previous work.[55]

As has been emphasized in the previous report, the geometry and characteristic of this simulated eye globe have been determined in a manner that the dimension and specification of

TABLE 1. Monte Carlo simulation uncertainties. The uncertainty of the Monte Carlo simulated dose distribution is attributed to statistical fluctuation of the simulation that is given in the output of the simulated data, source geometry, photoionization, cross section, and source energy simulated data, spectrum, which are calculated using the guidelines published in TG-43U1 report and some other publications.[64]

Component	*r = 1 cm*	*r = 5 cm*
Statistics[a]	0.5%	1.0%
Photoionization	1.5%	4.5%
Cross section (2.3%)		
Seed geometry	2.0%	2.0%
Source energy spectrum[a]	0.1%	0.3%
Quadrature sum	2.5%	5.0%

[a] On the transverse plane of a single source.

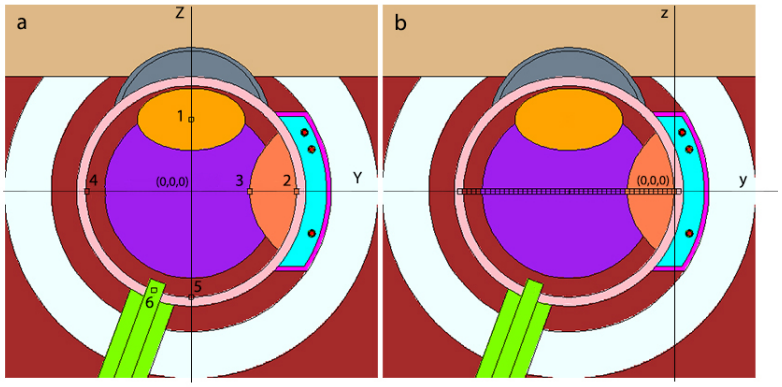

FIG. 1. The longitudinal cross-sectional diagram of the simulated human eye. In the left panel (a), the origin of the eye coordinate system is located at the center of the eye phantom. The voxels (numbered 1 to 6) indicate the lens, sclera, tumor apex, opposite side, macula, and optic nerve, respectively. In right panel (b), the origin of the plaque coordinate is at the interior surface of the sclera. The tally cells on this figure are shown along the central axis of the plaque, starting from sclera near the plaque to the sclera at the opposite side of the eye.

main parts of the human eye could be in conformity with the medical data.[54-63] The chemical compositions and densities of different components of the eyeball tissues which were used in these simulations are given in Table 2. Due to the nervous complexity of the retina and the vascular complexity of the choroid, their density and chemical compositions were assumed to be the same as water. A brief description of the components and shapes of the eyeball used in these simulations are given in the following section.

The dimensions of the adult human eyeball are relatively constant and may vary by only one or two millimeters, from one person to another. Normally, an adult eyeball has an anterior-to-posterior diameter of 24 millimeters, but the vertical and horizontal diameters are approximately 23 mm and 23.5 mm, respectively. Therefore, a spherical shell of 24.6 mm has been considered as an eye globe, during these simulations. In these simulations, the common volume between four concentric spheres with radii of 0.93, 1.03, 1.13, and 1.23 cm (centered at the center of the eye) are the introducer of retina, choroid and sclera, (three primary layers of the eye), respectively. The vitreous humor fills the space between the lens and the smallest sphere (the inner surface of the retina). The lens was defined as an ellipsoidal shape with equatorial diameters of 8 mm and 9 mm and a polar diameter of 0.25 cm. Also, the optic nerve has been defined as the volume between two concentric cylinders with diameters of 7 mm and 8 mm, which was located at the outer layer of the sclera. The skull bone has been simulated by considering the volume between two concentric spheres (centered at the origin of the eye coordinate) with radii of 1.505 cm and 2.05 cm. In both water and human eye globe phantom, the array of $0.5 \times 0.5 \times 0.5$ mm^3 voxels have been utilized for scoring the average energy deposition to different

TABLE 2. Elemental compositions and densities of different parts of the human eye-ball, water, and dry air used in this simulation.[54,57-62]

Material	Material Elemental Composition (% by mass)												Density (g/cm^3)
	H	*O*	*C*	*N*	*Na*	*Mg*	*P*	*S*	*Ar*	*Cl*	*K*	*Ca*	
Water	11.11901	88.8099	---	---	---	---	---	---	---	---	---	---	0.9980
Dry air	---	23.17812	0.012425	75.52673	---	---	---	---	1.282725	---	---	---	0.0012
Lens	9.60	64.60	19.50	5.70	0.10	---	0.10	0.30	---	0.10	---	---	1.07
Sclera	9.60	74.40	9.90	2.20	---	0.50	2.20	0.90	---	0.30	---	---	1.09
Vitreous	11.0867	88.052	0.068	---	0.2647	0.0025	0.002	---	---	0.502	0.0171	0.005	1.00
Aques humor	11.085	88.06	0.056	0.00001	0.348	0.0025	0.0018	0.00001	---	0.432	0.00798	0.0067	1.01
Optic nerve	10.70	76.70	9.50	1.80	0.20	---	0.30	0.20	---	0.30	0.30	---	1.039
Skull bone	5.00	43.50	21.20	4.00	0.10	0.20	8.10	0.30	---	---	---	17.60	1.61
Tumor	10.8	83.2	4.10	1.10	---	0.30	---	0.10	---	0.40	---	---	1.03

points in the eyeball (Fig. 1(b)). We have examined that the use of smaller voxel size (i.e., $0.1 \times 0.1 \times 0.1$ mm^3) will lead to similar results, but with much longer run time on computer, in order to achieve similar statistical uncertainties. Therefore, this voxel size (i.e., $0.5 \times 0.5 \times 0.5$ mm^3) was utilized for the final data collection. These tally cells are selected along the central axis of the plaque, starting from sclera near the plaque to the sclera at the opposite side of the plaque.

A single source dosimetry of Model 6711 ^{125}I source was used to validate the accuracy of the source and phantom geometry used in these Monte Carlo simulations. TG-43[64-65] recommended dosimetric characteristics of the single source (i.e., dose rate constant, radial dose function, and 2D anisotropy function) were compared with the published data for this validation process. These simulations were performed using a single source located at the center of a $30 \times 30 \times 30$ cm^3 water phantom. To calculate the dose falloff of the source, along its transverse axis with the smaller statistical fluctuations, toroid tally cells (torus-shaped cells) were selected. The major radii of these cells were chose to be in the range of 0.05 cm to 10 cm. The minor radii of the toroid cells, "R", varied as a functional of radial distance as: R = 0.008 cm for $0.05 < r \leq 0.1$; R = 0.01 cm for $0.1 < r \leq 1$ cm; R = 0.05 cm for $1 < r \leq 5$; and R = 0.1 cm for $5 < r \leq 10$ cm.

In the Monte Carlo calculations of this project, the simulations for air kerma rates are performed with the tally cells for scoring the collisional kerma at various distances relative to the source center. The calculated air kerma rates have been scored in the toroid cells filled with the dry air and located at distances ranging from 0.05 cm to 20 cm in vacuum and F6 tally was used. The air kerma strength (SK) is defined as the product of the air kerma rate at a given distance from the source center in vacuum by the square of the distance, as defined in the TG-43U1 recommendation. The SK is independent from the distance. The air kerma strength was then calculated for all the distances and has been found to be constant from 1 cm to 10 cm with relative statistical uncertainties less than 0.1%, so the average value in this region has been taken as the air kerma strength per history.

B. Choroidal melanoma

Choroidal melanoma is one of the three kinds of the uvea melanoma (choroidal, ciliary body, and iris melanoma). Treatment of the intraocular tumor depends on its basal diameter and apical height. Plaque brachytherapy can be used for the treatment of tumors with the apical height of 2.5 to 10 mm and the basal diameter of 16 mm or less.

In this work, a choroidal melanoma tumor with the apical height of 5 mm (i.e., 6 mm from the exterior surface of the sclera, according to COMS definition for the point of dose prescription[66]) has been simulated in both phantoms. This tumor has been assumed to be on the lateral portion to the eyeball on the equator.

C. Ophthalmic plaque and brachytherapy source

In these investigations, a fully-loaded 16 mm COMS eye plaque, containing 13 ^{125}I (model 6711, GE Healthcare/Oncura) brachytherapy sources have been modeled. These sources were sandwiched between a gold plaque with a density of 15.8 g/cm^3 and Silastic (Dow Corning Corp., Midland, MI) seed carrier with a density of 1.12 g/cm^3. The geometric information and composition of the simulated plaque were obtained from some published references.[67-72] Also, the coordinates of the 13 seeds for this plaque are in accordance with the standard position for COMS plaque.[66] Moreover, the detailed geometric and characteristic information of the model 6711 ^{125}I sources have been obtained from the publicly accessible website of the Carleton Laboratory for Radiotherapy physics seeds database.[73] The photon spectra quoted in TG-43[64] has been used to sample the initial photon energies and probabilities for these brachytherapy sources. In these simulations, both water and human eyeball phantom with the fully loaded eye plaque were placed in a $30 \times 30 \times 30$ cm^3 water phantom, for the final dosimetric evaluations. The location of the eyeball in this phantom was selected such that it nearly represented the real patient anatomy (i.e., the cornea of the eye was toward one surface of the cubical phantom).

D. Gold nanoparticles (GNPs)

In our simulation, 50 nm GNPs were uniformly distributed within the tumor, in both the eye phantoms filled with the water and the eye composition to create different concentrations (i.e., milligram of GNPs per gram of the target tissue) of 7, 10, 18, and 30 mg/g. From the simulated absorbed dose to different points of interests in the eyeball, with and without the presence of the GNPs, the values of the dose enhancement factors were calculated. Considering a treatment time of 100 hrs, a procedure introduced by Thomson et al.[54] was utilized to achieve a dose of 85 Gy at the tumor apex.

III. RESULTS

A. Calculation of TG-43 parameter (single source)

The accuracy of the seed model used in this study has been benchmarked via calculations of the TG-43 dosimetry parameters (air kerma strength, dose rate constant, and radial dose function) and comparison with the published results reported by Taylor and Rogers[73] and Rivard et al.[64]

Table 3 and Fig. 2 shows excellent agreement (within ± 5%) between the presently calculated radial dose function (RDF) of a single Oncoseed ^{125}I (Model 6711) brachytherapy source and the reported data by the Rivard and Taylor studies.

Moreover, the dose rate at the reference point (r_0 = 1 cm, $\theta_0 = \pi/2$) has been calculated, $\dot{D}(r_0, \theta_0)$, as the dose to water per photon history in a torus tally cells with 0.01 cm minor cross sectional diameter. It should be noted that r_0 and θ_0 are the transverse axis polar coordinates relative to the source center. The dose rate constant, Λ, has been obtained as the ratio of the calculated dose rate to the air kerma strength (SK) with the unit of cGy.h^{-1}U^{-1}. The symbol U is the unit of air-kerma strength of the source and it is defined as 1U = 1 cGy.cm^2.h^{-1}. The result gained from this study and those reported by TG-43[64] and Taylor and Rogers[73] are listed in Table 4.

TABLE 3. A comparison between the simulated radial dose function, g(r), of the oncoseed 6711 source in this project with the published data by other investigators.

Distance from Source (cm)	*Radial Dose Function, g(r)*		
	This work	*Taylor and Rogers[73]*	*TG-43[64]*
0.05	1.115	1.139	----
0.06	1.050	1.094	----
0.07	1.068	1.08	----
0.08	1.069	1.077	----
0.09	1.071	1.078	----
0.10	1.050	1.08	1.055
0.15	1.064	1.089	1.078
0.20	1.066	1.096	----
0.25	1.062	1.096	1.082
0.30	1.059	1.093	----
0.40	1.050	1.086	----
0.50	1.075	1.075	1.071
0.60	1.060	1.062	----
0.70	1.040	1.048	----
0.75	1.040	1.042	1.042
0.80	1.030	1.035	----
0.90	1.012	1.018	----
1.0	0.995	0.998	1
1.5	0.900	0.909	0.908
2.0	0.800	0.813	0.814
2.5	0.710	0.721	----
3.0	0.615	0.633	0.632
3.5	0.550	0.557	----
4.0	0.472	0.484	0.496
4.5	0.406	0.419	----
5.0	0.361	0.361	0.364
5.5	0.310	0.313	----
6.0	0.267	0.269	0.270
6.5	0.230	0.231	----
7.0	0.199	0.198	0.199
7.5	0.172	0.171	----
8.0	0.143	0.146	0.148
8.5	0.123	0.125	----
9.0	0.104	0.107	0.109
9.5	0.092	0.0914	----
10.0	0.0762	0.0775	0.0803

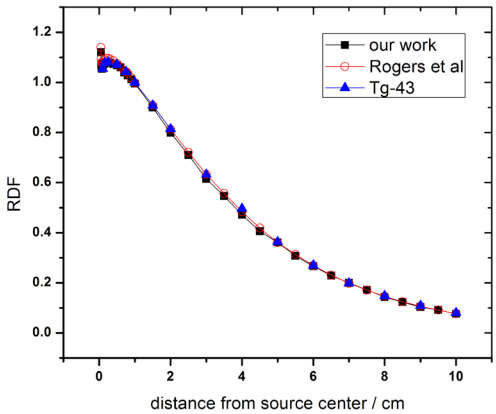

FIG. 2. Radial dose function for ^{125}I source with relative statistical uncertainties less than 1%. Voxel sizes are: 0.008 cm for distance between $0.05 < r \leq 0.1$, 0.01 cm for $0.1 < r \leq 1$ cm, 0.05 cm for $1 < r < 5$, and 0.1 cm for $5 < r \leq 10$. Circles and triangles are values calculated by Taylor and Rogers[73] and Rivard et al.[64]

Figure 3 displays the isodose contours in the x, y plane at z =0 for a 16 mm COMS plaque loaded with 13 ^{125}I Oncoseeds (Model 6711). This plaque has been simulated at the center of the water phantom and the dose has been scored in 0.1 cm^3 voxels. In this plot, the 100% line dose is located at the tumor apex. As the distance from this point increases, dose values decrease rapidly which is the main benefit of this treatment modality.

TABLE 4. A comparison of the dose rate constant, Λ (cGyU^{-1}h^{-1}), of ^{125}I brachytherapy source in water, simulated in this project with the published data.

	Taylor and Rogers[73]	*Rivard et al.*[64]	*This Work*
Dose rate constant	0.942	0.965	0.923±0.011

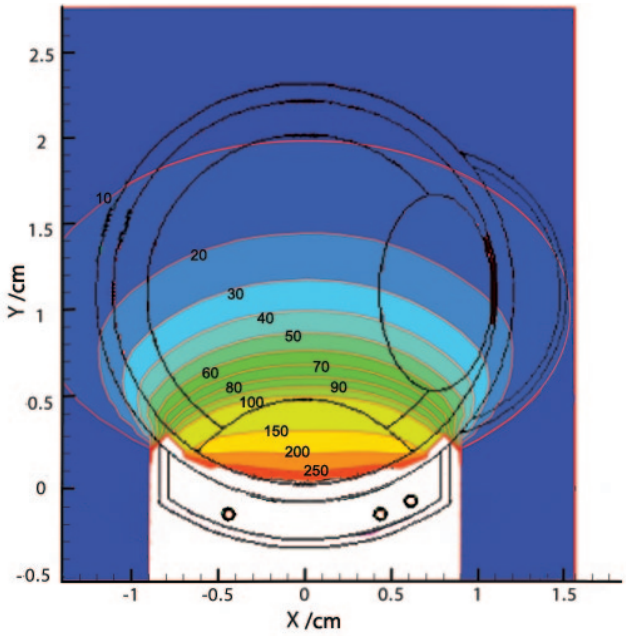

FIG. 3. Z-plane, 16 mm plaque (in water) isodose lines from MCNP, 100% at tumor apex.

B. Dosimetry calculations

Figure 4(a) shows the depth dose curve for ^{125}I sources in a fully loaded 16 mm COMS eye plaque in both water and eye phantoms (without the presence of the tumor), relative to the dose value at 5 mm depth (where in this work's tumor apex is assumed to be). These results show an agreement between the two sets of data for all the points, except the first and last points, that falls on the sclera adjacent to the plaque and opposite to the plaque, respectively. The dose value to the first and the end voxel in the eye phantom are approximately 26% higher than that of the voxels in water phantom. Based on the similarity between the elemental composition of the vitreous body and water, it is clear that the dose in the vitreous is approximately similar to that of the water. Moreover, the calculated depth dose in the water phantom has been compared with those calculated data by Thomson et al.[54] (Fig. 4(b)) with an excellent agreement (within the uncertainties shown in Table 1) between them.

Figure 4 shows the depth dose curves along the central axis direction of the plaque. To study the effect of the eyeball composition, the Monte Carlo simulation of the eye includes several 0.05 cm^3 voxels that have been selected at the different critical points in the eye, as well as the

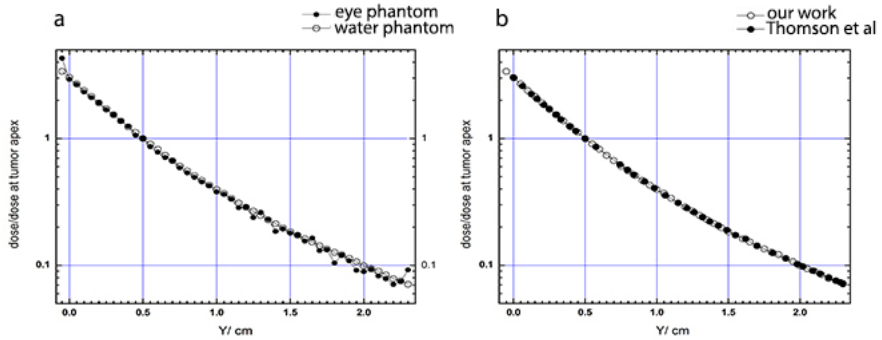

FIG. 4. The plaque central axis depth-dose curves (a) for ^{125}I in the water and the eye phantom. Comparison (b) of the plaque central axis depth dose in the water phantom between this work and the work by Thomson et al.[54] The vertical axis represents the ratio of dose to the dose at the tumor apex. The uncertainties are shown in Table 1.

tumor apex. With the assumptions and utilization of the approach of Thomson et al.,[54] the total dose at the points of interest have been calculated and they are shown in Table 5. The relative statistical uncertainty is lower than about 1% with the highest percent in the opposite side of the eye and the lowest percent in the sclera among the prescription points represented in this table. The calculated dose at points of interest for seeds in water and plaque in water has been compared with that reported by Thomson and colleagues. The air kerma strength per seed has been calculated for ^{125}I model 6711 following the method of the air kerma strength per seed introduced by other investigators.[53-54] Figure 5 presents a comparison between four concentrations of GNPs in the calculation of dose enhancement factor (DEF) in both phantoms. The dose enhancement factor has been plotted in the figure as a function of radial distances from the center of the plaque, while the plaque is placed next to the tumor in the simulated human eye and the water phantom.

Figure 6 shows the ratio of the central axis depth dose to the dose at the tumor apex for 16 mm COMS eye plaque in water phantom, eye globe, and simulated human eye with nanoparticles-induced tumor. These results show that for the same dose to the apex of the tumor lower normal tissue doses (distances > 0.5 cm which is the tumor apex) are achieved for larger concentration of the nanoparticles.

TABLE 5. A comparison of the integrated dose (Gy) at different points of interests in an eyeball, implanted with a 16 mm eye plaque located next to the tumor on the equator temporal to the eyeball. Columns labeled "P.W" and "S.W" compares the dose for 13 ^{125}I seeds in water phantom with and without the presence of the plaque, respectively. "Eye" refers to simulated human eye using the data of Table 2 and "water" refers to the simulated human eye in which all parts of the eye were assumed to be made of water. "Plaque in eye" refers to the 13 ^{125}I seeds with plaque present in human eye phantom. "7 mg/g, 10 mg/g, 18 mg/g, and 30 mg/g" refer to the concentration of GNPs inside the tumor in both phantom types. The relative statistical uncertainty is lower than 1%.

Location	*Thomson et al.*[54] *(S.W)*	*This Work (S.W)*	*Thomson et al.*[54] *(P.W)*	*This Work (P.W)*	*Plque in Eye*	*7 mg/g (water)*	*7 mg/g (eye)*	*10 mg/g (water)*	*10 mg/g (eye)*	*18 mg/g (water)*	*18 mg/g (eye)*	*30 mg/g (water)*	*30 mg/g (eye)*
Sclera	262.1	261.53	222.7	223.54	285.93	267.73	298.92	267.73	298.92	270.33	298.92	270.33	298.92
Apex	85.00	85.00	74.40	73.66	76.50	141.38	142.8	168.58	170.29	244.80	245.08	355.0	354.16
Center of eye	27.92	27.63	23.68	22.66	22.49	23.80	23.74	23.82	23.77	23.82	23.77	23.80	23.80
Opposite side	6.83	6.80	5.453	5.16	6.53	5.72	6.09	5.72	6.01	5.72	6.01	5.75	6.01
Optic disk	11.35	10.39	8.947	8.11	7.80	8.26	8.11	8.24	8.08	8.24	8.08	8.26	8.05
Lens	21.75	21.45	17.53	17.30	15.30	18.98	15.49	19.09	15.32	19.06	15.32	19.01	15.28
Macula	16.45	15.75	12.80	11.46	11.62	12.55	12.40	12.53	12.40	12.53	12.40	12.63	12.40

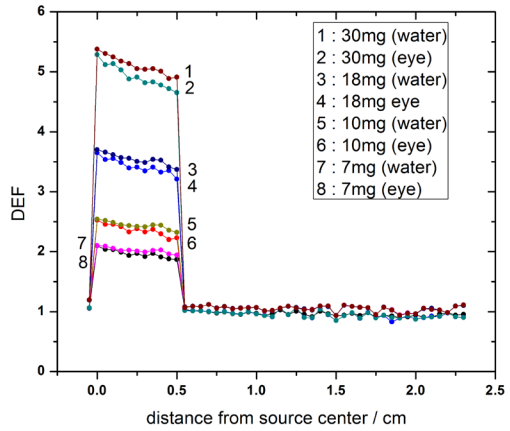

FIG. 5. The calculated dose enhancement factors for 50 nm GNPs within the tumor with concentrations of 7 mg/g, 10 mg/g, 18 mg/g, and 30 mg/g in the water and the eye model phantoms. For Monte Carlo simulation, the tally cells were placed along the central axis of the plaque, starting from the sclera near the plaque to the sclera opposite side of the plaque. DEF calculations have been done in the simulated human eye using the data shown in Table 2. Fully loaded 16 mm COMS eye plaque has been positioned next to the tumor on the equator temporal to the eyeball. A fully simulated human eye globe filled with eye material is referred to as (eye) and the water phantom is referred to as (water). The relative statistical uncertainty is lower than about 1%, with the highest percent in the opposite side of the eye and the lowest percent in the sclera among the prescription points represented in this table.

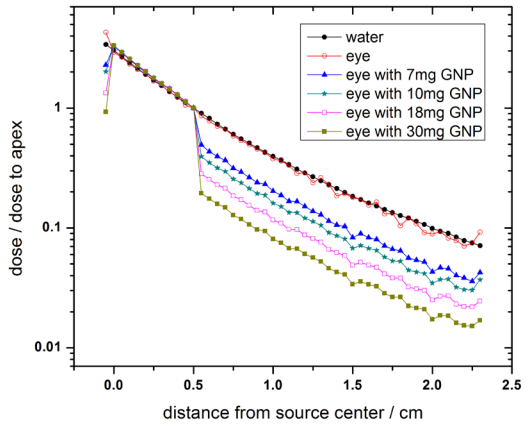

FIG. 6. The ratio of the full loaded 16 mm COMS eye plaque's depth doses to the dose at the tumor apex in the water phantom, simulated human eye, and simulated eye in which four concentrations of GNPs are defined inside the tumor. The uncertainties are as in Table 5.

IV. DISCUSSION

In radiation therapy, the required radiation dose for treatment is chosen based on the type of tumor and the rate of its progress. Determination of the required dose for the treatment of a specific tumor or the control of the tumor growth can be directly related to the treatment time for a given technique. For treatment of ocular melanoma, the prescribed dose is normally to the tumor apex. The height of the tumor apex may vary from patient to patient and, thus, the treatment time will vary, to deliver prescribed dose. These changes may affect the dose values to the normal tissues in the eye, such as sclera, optical nerve, and lens. Table 5 shows that defining the nanoparticles in the tumor area led to the dose increase inside the tumor with no significant changes in the absorbed dose by other parts of the eye in both phantom types. The calculated doses to the tumor apex in the presence of GNPs inside the tumor with the concentrations of 7 mg/g, 10 mg/g, 18 mg/g, and 30 mg/g was found to be increased by a factor of about 1.9, 2.2, 3.2, and 4.6, respectively, in the eye model and about 1.9, 2.3, 3.3, and 4.8 orders of magnitude, respectively, in the water phantom.

Despite the similarity of the dose enhancement to the tumor apex for the two phantom types, the results in Table 5 show that the composition of the eye materials influences the calculated dose in the choroidal melanoma. This effect is visible in the absence of GNPs, indicating that the dose to the points of interest in the eye phantom differs from that of water phantom. The dose to the center of lens and optic disk in the eye is lower than the dose calculated in these points in water. On the contrary, the dose to the sclera, apex, and the opposite side in the eye are more than that of the water phantom. The dose increase in the sclera is about 28% and the dose reduction in the lens is about 11.6%.

The differences between the results of dosimetry in the eye model and water phantom are more prominent when the GNPs are defined in the tumor. For example, in the presence of 18 mg/g GNPs, there is an increase of 20% in the eye model and 4% in the water phantom in the dose absorbed to sclera relative to that of the eye and water phantom with no nanoparticles present. These differences are mainly due to the impact of the elemental compositions of the two phantom types in the photoelectric interaction of the low energy photons from ^{125}I brachytherapy sources. Furthermore, with the presence of the plaque relative to the absence of the plaque, our results indicate that the dose to the point located opposite to the plaque has an increase of approximately 10% in the water phantom, while decreasing by about 7% in the eye phantom. This effect also can be attributed to the photoelectric interactions for the low energy photon and chemical elements of the two phantom types.

In Table 5, a comparison of the effect of the plaque for multiple seed simulation has been shown, too. The data show that the presence of the plaque around the seeds causes a decrease in the dose to all points of interest. For instance, the dose to the sclera and tumor apex in the water phantom in the presence of the plaque is about 14% less than that of the absence of the plaque, but with the same arrangement. This amount is increased as the distance from the plaque is increased. The dose reduction is a consequence of the elemental composition of the plaque backing gold alloy and the Silastic seed carrier. The high atomic number of the gold causes enhanced photoelectric absorption and results in a dose reduction. Table 5 shows that, in the presence of the plaque, the dose to sclera is approximately 28% larger in eye phantom than that of water phantom. The differences of the aforementioned increase of the dose values are due to the differences of the chemical compositions of the phantom material and presence of the plaque.

Regarding the results of Table 5 and considering the relative statistical uncertainty lower than about 1% in all calculations, the discrepancies between water and eye phantom are considerable in all parts of the eye. However, considering systematic uncertainties in eye plaque therapy, the discrepancies in some parts such as center of eye and macula may be in the range of uncertainties, and therefore they may not be reliable.

As can be seen from Fig. 5, the tumor dose enhancement is greater for higher concentration of GNPs in both water and the eye phantoms. However, the notable result is that at given concentrations of GNPs, the DEF value in the water phantom is larger than that in the eye phantom. Moreover, as shown in the figure, the difference between the eye and the water phantom increases with increasing nanoparticle concentration. Since the photoelectric cross section depends on the atomic number of the material and photon beam energy, the use of the ^{125}I as a low-energy photon source and GNP as a high-Z material will increase the probability of the photoelectric interaction inside the tumor. Therefore, as shown in Fig. 6, keeping a fixed prescribed dose delivery to the apex of the tumor will lead to a lower absorbed dose to the normal tissue of the eye. When the concentration of the nanoparticles increases in the area of the tumor, a higher amount of radiation energy will be absorbed in the tumor area due to an increase in the probability of the physical phenomena such as photoelectric. As a result, the amount of the dose absorbed by the normal tissue will be decreased.

V. CONCLUSIONS

In this study, a Monte Carlo simulation model of human eye was built, considering its composition closer to reality, and a water phantom was used to investigate the effects of the GNPs on radiation dose enhancement in ophthalmic brachytherapy dosimetry. The results show that a significant tumor dose enhancement could be achieved, using GNPs inside the tumor during the irradiation by low energy source. With a certain diameter of GNPs, the results of the dose calculation show a higher dose enhancement for the greater concentration of GNPs.

The presence of GNPs inside the tumor made no significant changes in the radiation-absorbing sensitivity of other normal tissue of the eye. Therefore, for the same delivery of the dose to the tumor apex, one may be able to deliver a smaller dose to the normal tissues in the eye (Fig. 6). Furthermore, comparing the dosimetry calculations in the presence of GNPs between the water phantom and the eye model shows the importance of a more accurate definition of the eye material in ophthalmic brachytherapy.

The results of the Monte Carlo study in this investigation show that the presence of GNPs inside the tumor could play an important role in dose enhancement. However, the availability of an experimental study (*in vitro* or *in vivo*) in melanoma could result in a better understanding of the effect of GNP in the melanoma dosimetry. A full experimental investigation of the effects of the GNPs inside the choroidal melanoma on brachytherapy dosimetry could answer many of the questions in this project.

REFERENCES

1. Jager MJ, Desjardins L, Kivela T, Damato BE, editors. Current concepts in Uveal Melanoma, 49: Developments in ophthalmology. Basel: Karger; 2012.
2. Simpson ER, Gallie B, Laperrierre N, et al. The American Brachytherapy Society consensus guidelines for plaque brachytherapy of uveal melanoma and retinoblastoma. Brachytherapy. 2014;13(1):1–14.
3. Augsburger JJ. Size classification of posterior uveal malignant melanomas. In: Laibson PR, editor. Yearbook of ophthalmology. Maryland Heights, MO: Mosby; 1993.
4. Collaborative Ocular Melanoma Study Group. The Collaborative Ocular Melanoma Study (COMS) randomized trial of pre enucleation radiation of large choroidal melanoma I: characteristics of patients enrolled and not enrolled. COMS report no. 9. Am J Ophthalmol. 1998;125(6):767–78.
5. Warren RM. Prognosis of malignant melanomas of the choroid and ciliary body. Current Concepts in Ophthalmology. 1974;4:158–67.
6. Damato B. Developments in the management of uveal melanoma. Clin Experiment Ophthalmol. 2004;32(6):639–47.
7. Meigooni AS. Recent developments in brachytherapy source dosimetry. Iran J Radiat Res. 2004;2(3):97–105.
8. Zhang L, Chen H, Wang L, et al. Delivery of therapeutic radioisotopes using nanoparticle platform: potential benefit in systemic radiation therapy. Nanotechnol Sci Appl. 2010;3:159–70.
9. Finger PT. Radiation therapy for choroidal melanoma. Surv Ophthalmol. 1997;42(3):215–32.

10. Simpson ER. Uveal melanoma: approaches to management, Chapter 15. In: Keretes PJ and Jahnson TM, editors. Evidence-based eye care. Philadelphia, PA: Lippincott Williams & Wilkins; 2007.
11. Puusaari I, Heikkonen J, Summanen P, Tarkkanen A, Kivela T. Iodine brachytherapy as an alternative to enucleation for large uveal melanomas. Ophthalmology. 2003;110(11):2223–34.
12. Stallard HB. Radiotherapy for malignant melanoma of the choroid. Br J Ophthalmol. 1966;50(3):147–55.
13. Leonard KL, Gagne NL, Mignano JE, Duker JS, Bannon EA, Rivard MJ. A 17-year retrospective study of institutional results for eye plaque brachytherapy of uveal melanoma using ^{125}I, ^{103}Pd, and ^{131}Cs and historical perspective. Brachytherapy. 2011;10(4):331–39.
14. Cho S, Jeong J. H, Kim C. Monte Carlo simulation study on dose enhancement by gold nanoparticles in brachytherapy. J Korean Phys. 2010;56(6):1754–58.
15. Green JA. Optimization of eye plaque dosimetry using Monte Carlo method [MSc thesis]. School of engineering physics, University of Wollongong. Wollongong, Australia: University of Wollongong; 2011.
16. Collaborative Ocular Melanoma Study Group. COMS study forms book. Springfield, VA: National Technical Information Service; 1998.
17. Zheng Y, Hunting DJ, Ayotte P, Sanche L. Radiosensitization of DNA by gold nanoparticles irradiated with high-energy electrons. Radiat Res. 2008;169(1):19–27.
18. Brualla L, Zaragoza FJ, Sauerwein W. Monte Carlo simulation of the treatment of eye tumors with ^{106}Ru plaques: a study on maximum tumor height and eccentric placement. Ocul Oncol Pathol. 2015;1(1):2–12.
19. Sanches-Rayes A, Tello J, Guix B, Salvat F. Monte Carlo calculation of the dose distributions of two ^{106}Ru eye applicators. Radiother Oncol. 1998;49(2):191–96.
20. Brualla L, Sempau J, Sauerwein W. Comment on Monte Carlo calculation of the dose distributions of two ^{106}Ru eye applicators [Radiother Oncol. 1998;49(2):191–96]. Radiother Oncol. 2012;104(2):267–68.
21. Cross W, Hokkanen J, Jarvinen H, et al. Calculation of beta-ray dose distributions from ophthalmic applicators and comparison with measurements in a model eye. Med Phys. 2001;8(7):1385–96.
22. Mourtada F, Koch N, Newhauser W. ^{106}Ru/^{106}Rh plaque and proton radiotherapy for ocular melanoma: a comparative dosimetric study. Radiat Prot Dosimetry. 2005;116(1-4):454–60.
23. Fuss MC, Muñoz A, Oller JC, et al. Energy deposition by a ^{106}Ru/^{106}Rh eye applicator simulated using LEPTS, a low-energy particle track simulation. Appl Radiat Isot. 2011;69(9):1198–204.
24. Hermida-López M. Calculation of dose distributions for 12 ^{106}Ru/^{106}Rh ophthalmic applicator models with the PENELOPE Monte Carlo Code. Med Phys. 2013;40(10):101705.
25. Brualla L, Sempau J, Zaragoza FJ, Wittig A, Sauerwein W. Accurate estimation of dose distributions inside an eye irradiated with ^{106}Ru plaques. Strahlenther Onkol. 2013;189:68–73.
26. Zhang XD, Guo ML, Wu HY, et al. Irradiation stability and cytotoxicity of gold nanoparticles for radiotherapy. Int J Nanomed. 2009;4:165–73.
27. Cai W, Gao T, Hong H, Sun J. Application of gold nanoparticles in cancer nanotechnology. Nanotech Sci Appl. 2008;1:17-32.
28. Chang MY, Shiau AL, Chen YH, Chen HH, Wu CL. Increased apoptotic potential and dose-enhancing effect of gold nanoparticles in combination with single-dose clinical electron beams on tumor-bearing mice. Cancer Sci. 2008;99(7):1479–84.
29. Hainfeld JF, Dilmamian FA, Slatkin DN, Smilowitz HM. Radiotherapy enhancement with gold nanoparticles. J Pharm Pharmacol. 2008;60:977–85.
30. Huang X, Jain PK, El-Seyed IH, El-Seyed MA. Gold nanoparticles: interesting optical properties and recent applications in cancer diagnostic and therapy. Nanomedicine. 2007;2(5):681–93.
31. Cho SH. Estimation of tumor dose enhancement due to gold nanoparticles during typical radiation treatments: a preliminary Monte Carlo Study [abstract]. Med Phys. 2005;32(6):2162.
32. Hainfeld JF, Slatkin DN, Smilwitz HM. The use of gold nanoparticles to enhance radiotherapy in mice. Phys Med Biol. 2004;49(18):309–15.
33. Zhang XD, Xing JZ, Chen J, et al. Enhanced radiation sensitivity in prostate cancer by gold-nanoparticles. Clin Invest Med. 2008;31(3):160–67.
34. Liu GJ, Wang CH, Chen ST, et al. Enhancement of cell radiation sensitivity by pegylated gold nanoparticles. Phys Med Biol. 2010;55(4):931–45.
35. Chithrani DB, Jelveh S, Jalali F, van Prooijan M, Allen C, Bristow RG. Gold nanoparticles as radiation sensitizers in cancer therapy. Radiat Res. 2010;173(6):719–28.
36. Hainfeld JF, Dilmanian FA, Zhong Z, Kaler-Ezra JA, Smilowitz HM. Gold nanoparticles enhance the radiation therapy of a murine squamous cell carcinoma. Phys Med Biol. 2010;55(11):3045–59.
37. Sim L, Fielding A, English M, et al. Enhancement of biological effectiveness of radiotherapy treatments of prostate cancer cells in vitro using gold nanoparticles. Presented at the 2011 International Nanomedicine Conference, 14-16th July 2011, Coogee Beach, Sydney, N.S.W.
38. Cho SH, Jones BL, Krishnan S. The dosimetric feasibility of gold nanoparticle-aided radiation therapy (GNRT) via brachytherapy using low-gamma/X-ray source. Phys Med Biol. 2009;54(16):4889–905.
39. Maeda H, Wu J, Sawa T, Matsumura Y, Hori K. Tumor vascular permeability and the EPR effect in macromolecular therapeutics. A review. J Control Release. 2000;65(1-2):271–84.
40. Nordiana RW, Nour B, Trevor A, et al. Enhancement of radiation effects by gold nanoparticles for superficial radiation therapy. Nanomed Nanotech. 2009;5:136–42.
41. Ngwa W, Korideck H, Kassis AL, et al. In vitro radiosensitization by gold nanoparticles during continuous low-dose-rate gamma irradiation with I-125 brachytherapy seeds. Nanomed Nanotech. 2013;9(1):25–27.
42. Chow JC, Leung MK, Fahey S, Chithrani DB, Jaffray DA. Monte Carlo simulation on low-energy electrons from gold nanoparticle in radiotherapy. J Physics: Conference Ser. 2012;341(1):012012.

43. Zhang XZ, Gao J, Buchholz TA, et al. Quantifying tumor-selective radiation dose enhancements using gold nanoparticles: a Monte Carlo simulation study. Biomed Microdevices. 2009;11:925–33.
44. Ghorbani M, Pakravan D, Bakhshabadi M, Meigooni AS. Dose enhancement in brachytherapy in the presence of gold nanoparticles: a Monte Carlo study on the size of gold nanoparticles and method of modelling. Nukleonika. 2012;57(3):401–06.
45. Letchman E, Chttopndhyay N, Cai Z, Mashouf S, Reilly R, Pignol JP. Implications on clinical scenario of gold nanoparticle radiosensitization in regards to photon energy, nanoparticle size, concentration and location. Phys Med Biol. 2011;56(15):4631–37.
46. Leung MK, Chow JC, Chithran BD, Lee MJ, Oms B, Jaffray DA. Irradiation of gold nanoparticles by X-rays: Monte Carlo simulation of dose enhancement and the spatial properties of the secondary electrons production. Med Phys. 2011;38(2):624–31.
47. Cho SH. Estimation of tumor dose enhancement due to gold nanoparticles during typical radiation treatment: a preliminary Monte Carlo Study. Phys Med Biol. 2005;50(15):163–73.
48. Amato E, Italiano A, Leotta S, Pergolizzi S, Torrisi L. Monte Carlo study of the dose enhancement effect of gold nanoparticles during x-ray therapies and evaluation of the anti-angiogenic effect on tumour capillary vessels. J X-ray Sci Technol. 2013;21(2):237–47.
49. Zhang S, Zhou J, Hu Z, Nair A, Tang L. Nanoparticles for uveal melanoma treatment. Proc IEEE Conf Nanotechnol. 2008:822–25.
50. Kang SJ, Durairaj CH, Kompella UB, O'Brien JM, Grossniklaus HE. Subconjunctival nanoparticle carboplatin in the treatment of murine retinoblastoma. Arch Ophthalmol. 2009;127(8):1043–47.
51. X-5 Monte Carlo Team. MCNP—a general Monte Carlo N-Particle transport code, version 5. Los Alamos, NM: Los Alamos National Laboratory; 2003.
52. ENDF-201 ENDF/B-VI summary documentation, Brookhaven National Laboratory Report BNL.NCS-17541, 8th ed. Upton, NY: National Nuclear Data Center; 2000.
53. Zhang H, Baker C, McKinsey R, Meigooni A. Dose verification with Monte Carlo technique for prostate brachytherapy implants with ^{125}I sources. Med. Dosim. 2005;30(2):85–91.
54. Thomson RM, Taylor RE, Rogers DW. Monte Carlo dosimetry for ^{125}I and ^{103}Pd eye plaque brachytherapy. Med Phys. 2008;35(12):5530–43.
55. Asadi S, Masoudi SF, Shahriari M. The effects of variations in the density and composition of eye materials on ophthalmic brachytherapy dosimetry. Med Dosim. 2012;37(1):1–4.
56. Lesperance M, Martino M, Thomson RM. Monte Carlo dosimetry for ^{103}Pd ^{125}I, and ^{131}Cs ocular brachytherapy with various plaque models using an eye phantom. Med Phys. 2014;41(3):031706.
57. Yanoff M and Duker JS. Ophthalmology, 3rd edition. Maryland Heights, MO: Mosby; 2009.
58. ICRU. Photon, electron, photon and neutron interaction data for body tissues. ICRU Report 46. Washington, DC: ICRU; 1986.
59. Kaufman PL, Alm A, Adler FH. Adler's physiology of the eye: clinical application. St. Louis, MO: Washington University School of Medicine; 2011.
60. Peratta A. 3D low frequency electromagnetic modeling of the human eye with boundary elements. Eng Anal Boundary Elem. 2008;32(9):726–35.
61. Cibis G. 2008-2009 Basic and clinical science course. Sections 2: Fundamentals and principles of ophthalmology. San Francisco, CA: Am Acad Ophthalmology; 2008.
62. Duck FA. Physical properties of tissue: a comprehensive reference book. London: Academic Press; 1990.
63. Yoriyaz H, Sanchez A, dos Santos A. A new human eye model for ophthalmic brachytherapy dosimetry. Radiat Prot Dosimetry. 2005;115(1-4):316–19.
64. Rivard MJ, Coursey BM, DeWerd LA, et al. Update of AAPM Task Group No. 43 Report: a revised AAPM protocol for brachytherapy dose calculations. Med Phys. 2004;31(3):633–74.
65. Nath R, Anderson LL, Luxton G, Weaver KA, Williamson JF, Meigooni AS. Dosimetry of interstitial brachytherapy sources: recommendations of the AAPM Radiation Therapy Committee Task Group No. 43. Med Phys. 1995;22(2):209–34.
66. Chiu-Tsao ST, Astrahan MA, Finger PT, et al. Dosimetry of ^{125}I and ^{103}Pd COMS eye plaques for intraocular tumors: report of Task Group 129 by the AAPM and ABS. Med Phys. 2012;39(10):6161–84.
67. Chiu-Tsao ST. Episcleral eye plaques for treatment of intraocular malignancies and benign diseases. Presented at the ABS AAPM Summer School, Seattle, 2005.
68. Puusaari I, Heikkonen J, Kivela T. Effect of radiation dose on ocular complications after iodine brachytherapy for large uveal melanoma; empirical data and simulation of collimating plaques. Invest Ophthalmol Visual Sci. 2004;45(10):3425–34.
69. Astrahan MA, Luxton G, Jozsef G, Liggett PE, Petrovich Z. Optimization of ^{125}I ophthalmic plaque brachytherapy. Med Phys. 1990;17(6):1053–57.
70. Collaborative Ocular Melanoma Study Group (COMS). The COMS randomized trial of iodine-125 brachytherapy for choroidal melanoma, II. Characteristics patients enrolled and not enrolled. COMS report No. 17. Arch Ophthalmol. 2001;119(17):951–65.
71. Sources and their application in brachytherapy. J ICRU. 2004;4(2):21–27.
72. Kim JH and Hilaris B. Iodine-125 source in interstitial tumor therapy. Clinical and biological considerations. AJR Am J Roentgenol. 1975;123(1):163–69.
73. Taylor RE and Rogers DW. The CLRP TG-43 parameter database for brachytherapy. Ottawa, ON: Carleton Laboratory for Radiotherapy Physics; 2013. Accessible at: http://www.physics.carleton.ca/clrp/seed_database